J. Fluid Mech. (2009), *vol.* 624, *pp.* 389–411.
doi:10.1017/S0022112008005612 Printed in the United Kingdom

On separated shear layers and the fractal geometry of turbulent scalar interfaces at large Reynolds numbers

FAZLUL R. ZUBAIR AND HARIS J. CATRAKIS†

Mechanical and Aerospace Engineering, University of California, Irvine, CA 92697, USA

(Received 2 March 2008 and in revised form 18 December 2008)

This work explores fractal geometrical properties of scalar turbulent interfaces derived from experimental two-dimensional spatial images of the scalar field in separated shear layers at large Reynolds numbers. The resolution of the data captures the upper three decades of scales enabling examination of multiscale geometrical properties ranging from the largest energy-containing scales to inertial scales. The data show a $-5/3$ spectral exponent over a wide range of scales corresponding to the inertial range in fully developed turbulent flows. For the fractal aspects, we utilize two methods as it is known that different methods may lead to different fractal aspects. We use the recently developed method for fractal analysis known as the Multiscale-Minima Meshless (M^3) method because it does not require the use of grids. We also use the conventional box-counting approach as it has been frequently employed in various past studies. The outer scalar interfaces are identified on the basis of the probability density function (p.d.f.) of the scalar field. For the outer interfaces, the M^3 method shows strong scale dependence of the generalized fractal dimension with approximately linear variation of the dimension as a function of logarithmic scale, for interface-fitting reference areas, but there is evidence of a plateau near a dimension $D \sim 1.3$ for larger reference areas. The conventional box-counting approach shows evidence of a plateau with a constant dimension also of $D \sim 1.3$, for the same reference areas. In both methods, the observed plateau dimension value agrees with other studies in different flow geometries. Scalar threshold effects are also examined and show that the internal scalar interfaces exhibit qualitatively similar behaviour to the outer interfaces. The overall range of box-counting fractal dimension values exhibited by outer and internal interfaces is $D \sim 1.2$–1.4. The present findings show that the fractal aspects of scalar interfaces in separated shear layers at large Reynolds number with $-5/3$ spectral behaviour can depend on the method used for evaluating the dimension and on the reference area. These findings as well as the utilities and distinctions of these two different definitions of the dimension are discussed in the context of multiscale modelling of mixing and the interfacial geometry.

1. Introduction

The geometrical, and possibly fractal, nature of turbulence continues to be an unresolved fundamental and practical problem persisting from theoretical proposals by Mandelbrot (1975) to many subsequent studies (e.g. Antonia & Sreenivasan 1977; Sreenivasan 1985, 1991; Sreenivasan, Ramshankar & Meneveau 1989; Meneveau &

† Email address for correspondence: catrakis@gmail.com

Sreenivasan 1991; Anselmet, Djeridi & Fulachier 1994; Dahm & Dowling 1996, 1997, 1998; Dahm & Southerland 1997; Su & Clemens 1999; Catrakis 2000, 2004, 2008; Brethouwer, Hunt & Nieuwstadt 2003; Dasi, Schuerg & Webster 2007; Bermejo-Moreno & Pullin 2008). Examination and analysis of scalar interfaces generated especially in large-Reynolds-number flows is important in a wide range of fundamental problems as well as applications that involve physical phenomena across the interfaces such as molecular diffusion, chemical reaction, bioluminescence or electromagnetic wave propagation (Pope 1988, 2000; Joseph & Preziosi 1989; Sreenivasan 1991, 1999, 2004; Villermaux & Innocenti 1999; Warhaft 2000; Bisset, Hunt & Rogers 2002; Bilger 2004; Catrakis 2004; Latz *et al.* 2004; Aguirre & Catrakis 2005; Dimotakis 2005; Schumacher, Sreenivasan & Yeung 2005). Therefore, it is desirable to develop a general understanding of the physical features of these scalar interfaces. Additionally, fundamental knowledge of interfacial properties provide clues to the distribution of physical scales in turbulent flows (Sreenivasan, Prabhu & Narasimha 1983; Catrakis 2000). Geometrical interfacial properties such as fractal dimensions are useful for the development of physical models for scale-local and scale-cumulative quantities, in addition to the spectral behaviour of turbulent phenomena (Sreenivasan 1991; Trouvé & Poinsot 1994; Schumacher & Sreenivasan 2003). Since turbulent interfaces are highly irregular and dynamic, there are significant challenges in their modelling, examination and optimization.

Theoretically, Mandelbrot (1975) was the first to argue that the fractal dimension of turbulent scalar isosurfaces or scalar interfaces is $8/3$ for the Kolmogorov spectral exponent of $-5/3$. However, in the subsequent decades of studies, there have been various reports on fractal dimensions of not only this value but other values and even scale-dependent fractal dimensions (e.g. Sreenivasan 1991; Catrakis 2000; Dasi *et al.* 2007). A large number of reports based on box counting have indicated a constant dimension of approximately 2.35 (e.g. Sreenivasan 1991). However, there are various other reports that appear to indicate scale-dependent behaviour for the generalized fractal dimension, i.e. a fractal dimension that depends on scale (e.g. Catrakis, Aguirre & Ruiz-Plancarte 2002*a*; Dasi *et al.* 2007). Possible interpretations of findings of scale dependence include finite-Reynolds-number effects (e.g. Catrakis 2000), non-fractal inclusions (e.g. Frederiksen *et al.* 1997), large-scale effects (Catrakis *et al.* 2002*a*) or non-fractal level crossing statistics (e.g. Catrakis 2000). It is also important to keep in mind that different definitions of a geometrical, or fractal, dimension can lead to different results as emphasized, for example, by Sreenivasan (1991).

This paper focuses on geometrical properties of scalar turbulent interfaces derived from large-Reynolds-number separated shear layers. Three new key elements in this work are the flow geometry that has not been previously explored for fractal aspects, the large-Reynolds-number conditions which are higher than many previous studies of fractals (e.g. Catrakis *et al.* 2002*b*) and the use of two different methods for evaluating the fractal dimension where one of the methods has been recently developed (Catrakis 2008). We show results on the scalar power spectrum and the p.d.f. of the scalar field. The latter enables identification of scalar thresholds corresponding to upper and lower outer interfaces, as well as intermediate thresholds corresponding to internal interfaces. We then show results on the generalized fractal dimension of scalar interfaces using two different methods for evaluating the dimension as a function of scale. Section 2 gives a description of our experimental facility and imaging technique. Section 3 describes the recently developed method of exploring the geometric behaviour of interfaces known as the M^3 method pioneered by Catrakis (2008) which is based on earlier theoretical work in this field (Catrakis 2000). Section 4 presents the results of the fractal analysis of the shear layer interfaces using both the M^3 method and

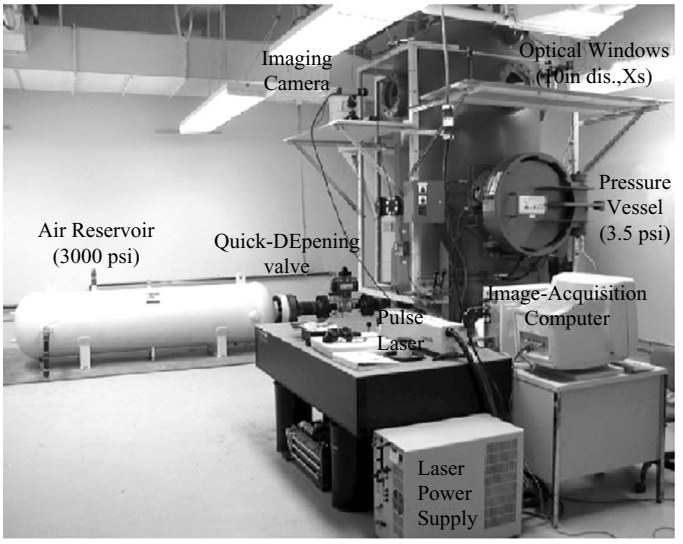

FIGURE 1. Photograph of the variable pressure flow facility at UC Irvine. The main pressure vessel is visible in the right part of the photograph. It has a large interior and cross section, extensive optical access and a quick-release door, to facilitate investigations of turbulent flows at variable pressures. Combined with laser and camera diagnostics, this facility enables high-resolution imaging of separated shear layers at large Reynolds numbers. The blow-down wind tunnel and test section are housed inside the main vessel.

the box-counting method. In Section 4, we will see that the M^3 method reveals scale-dependent behaviour in the generalized fractal dimension of the shear layer interfaces depending on the choice of the reference region utilized to contain the interfaces. However, the results using traditional box counting demonstrate evidence of fractal constant-dimension behaviour for the scalar interfaces. The effects of scalar threshold are also examined using both the M^3 method and the box-counting method. Finally, Section 5 discusses the key results and makes concluding remarks.

2. Experimental facility and procedure

The UC Irvine variable-pressure flow facility, utilized in the present investigations, can be seen in detail in figure 1. This facility allows experiments to be conducted at elevated test section pressures, in the range $1 \leqslant p \leqslant 20$ atm, which allows higher signal-to-noise ratio flow imaging than would be possible at atmospheric or sub-atmospheric pressures. For imaging techniques based on laser-induced fluorescence, such as the method presently used and described in this section, the resulting image signal-to-noise ratio is sufficiently high to enable an interface-based examination of the turbulent shear layers generated in the facility. This is due to the increased local density of air molecules as a result of conducting the experiment at higher operating pressures.

The laboratory facility primarily consists of a blow-down wind tunnel contained inside a large variable-pressure vessel. The main vessel, in which the wind tunnel is housed, is oriented upright and is shown on the right side of figure 1. The gas reservoir, which supplies fluid to the wind tunnel, is oriented horizontally and is shown on the left side of figure 1. The maximum supply pressure of the reservoir is 3000 psi or 200 atm. The maximum operating pressure of the vessel is 300 psi or 20 atm. For the flow conditions used in this experiment, the Reynolds number based on the visual thickness of the flow field is $Re \sim 6 \times 10^6$. A schematic illustration of

FIGURE 2. Schematic illustration showing the separated free shear layer. The larger box indicates the part of the flow that is shadowgraphed and the smaller box indicates the part of the scalar field of the shear layer that is imaged with laser-induced fluorescence.

the separated shear layer geometry is shown in figure 2 which indicates the region of the flow that is shadowgraphed and the region of the scalar field that is imaged with laser-induced fluorescence as discussed further below. The large scale of the shear layer at the laser-induced-fluorescence imaging location is the visual thickness which is $L \sim 0.1$ m.

The main vessel is 8 feet in height and 4 feet in diameter, easily enabling two people to stand in the interior when reconfiguring the test section or the tunnel. The main vessel has a quick-release entrance door of 2 feet in diameter that facilitates access in and out of the vessel. Both the main pressure vessel and the reservoir vessel are 'U'-stamp ASME rated. Two ellipsoidal cap sections, for each vessel, are welded at the two ends of the main cylindrical sections. Both vessels including the quick-release door mechanism were fabricated by Melco Steel. The main vessel and the reservoir vessel are equipped with NPT (National Pipe Tread) fittings for attachments of pressure gauges, vacuum lines, transducers and any other instrumentation necessary for flow management.

Extensive optical access to the interior of the main pressure vessel is available through five high-optical-quality spectrosil windows each with a diameter of 10 in and a thickness 3.25 in. Four of the five windows are vertical optical ports located on the four sides of the main pressure vessel. The fifth window is a horizontal optical port located on the top of the vessel. Combined with laser diagnostics, this facility is capable of quantitative high-resolution imaging of high-Reynolds-number turbulent flow fields.

The flow geometry currently examined is a separated turbulent shear layer (see figure 2) which is an example of a separated flow relevant in a wide range of problems (Kyrazis 1993; Morris & Foss 2003). In the present experiments, the flow is directed vertically upwards through the pressure vessel and the beam propagation is horizontal. The separated shear layer represents a basic flow configuration of interest for future studies where more complex flow geometries can be observed. For example, while separated flows over curved surfaces have an unsteady separation point, the sharp 90° corner defined in the present flow geometry ensures a fixed separation point. Studies of the unforced separated shear layer can provide valuable baseline information to evaluate the extent to which active flow control techniques including large-scale disorganization or regularization can be effective (Jumper & Fitzgerald 2001; Stanek *et al.* 2002).

In the present study, acetone vapour molecularly mixed in air is utilized. To generate the purely gaseous air/acetone mixture, a stream of air is passed through a liquid bath of acetone using the bubbling method (Thurber & Hanson 1999). The air/acetone mixture is supplied to the reservoir which is pressurized before each experimental run. The main vessel is pressurized with filtered air at $p \sim 3$ atm prior to releasing the reservoir gas into the blow-down tunnel and test section. The acetone-vapour

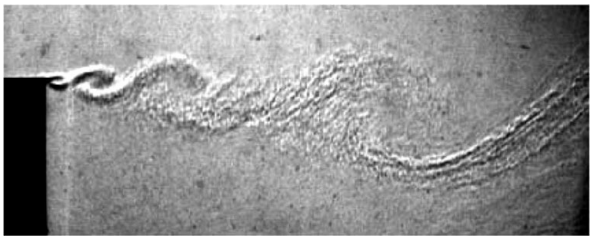

FIGURE 3. Example of a shadowgraph of the separated shear layer in the present flow facility.

concentration in air is regulated by controlling the mass flux of air through the bubbling unit. In the present experiments, an acetone-vapour concentration of 2 % by volume is generated in order to ensure negligible absorption of the laser energy, similar to previous experiments on laser-induced fluorescence (Catrakis *et al.* 2002), and in order to maintain conditions below the lower flammability limit of acetone. The resulting Schmidt number is $Sc \sim 1$ for the present case of purely gaseous acetone premixed in air that subsequently undergoes turbulent mixing in the shear layer with pure air. A shadowgraph of the separated shear layer is shown in figure 3.

The ultraviolet beam used in the present study is generated from a pulsed Nd:YAG laser. The illumination source employed is a moderate-energy laser system (Spectra Physics Model INDI 40–10) which produces 70 mJ ultraviolet light pulses at a wavelength of 266 nm. This wavelength corresponds to frequency quadrupling at the fourth harmonic of the illumination sources fundamental infrared 1064 nm output. The laser beam is shaped into a laser sheet with a width of 15 cm and a thickness of 150 μm. A parabolic mirror ensures that the laser sheet that is produced from the lens is of parallel extent before it propagates through the test section. The laser sheet is directed through the quartz windows of the pressure vessel and into the high Reynolds number separated shear layer. The laser-sheet orientation corresponds to a streamwise slice of the turbulent shear layer. The extent of the laser sheet that illuminates the shear layer is approximately 15 cm × 15 cm. The laser-sheet width of 15 cm corresponds to the downstream extent of the imaged flow field. The large-scale transverse extent of the shear layer at the imaging location is approximately $L \sim 10$ cm. The incident laser sheet excites the acetone vapour in the air to generate visible (blue) light through fluorescence. The elevated test section pressure of $p \sim 3$ atm results in a significant increase in the fluorescence signal, relative to atmospheric or sub-atmospheric test-section pressures, in agreement with previous studies (Thurber & Hanson 1999).

The laser-induced fluorescence signal is recorded on a high-resolution digital intensified charge-coupled device (CCD) camera with $\sim 1000^2$ pixels. The camera system is oriented along a direction normal to the incident laser sheet and, therefore, perpendicular to the laser propagation direction. The digital camera system employed is an intensified CCD camera by Stanford Photonics (Mega-10Z) with enhanced sensitivity in the blue visible spectrum. This enables the recording of the two-dimensional spatial slices of the acetone-vapour concentration field in the turbulent shear layer. An example of a scalar field image is shown in figure 4. The fluorescence-signal images are normalized and calibrated pixel-by-pixel using post-run images recorded at uniform concentration as well as pre-run images that correspond to pure air images in the test section. The normalization and calibration procedure is similar to the methods described in a previous study (Catrakis *et al.* 2002). In the present experiments, the turbulent mixing of the free stream gas (which contains a mixture of acetone and air) with the ambient gas (pure air) generates the scalar field

FIGURE 4. Example of a high-resolution image of the scalar field in a large-Reynolds-number separated shear layer recorded with laser-induced fluorescence.

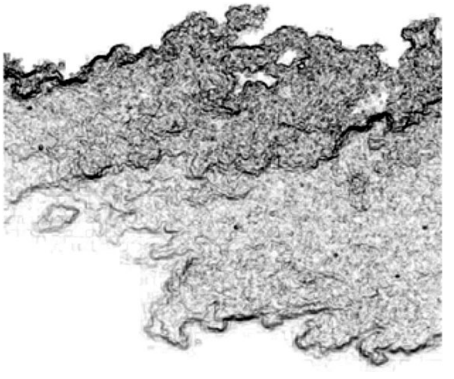

FIGURE 5. This image is an example of a visualization of figure 4, to further illustrate the geometrical complexity of the scalar field and interfaces, in which the dark regions of the image represent interfaces where the scalar in-plane gradient is large relative to the scalar in-plane gradient in the brighter regions.

corresponding directly to the acetone-vapour concentration field. Figure 5 shows a further visualization of the scalar field and interfaces from the example in figure 4 by depicting increasing values of the in-plane scalar gradient with darker regions, in order to illustrate the geometrical complexity of the scalar variations.

It is important to note that the laser-induced fluorescence images are high-resolution images, but they are not fully resolved. Because of this, this study does not include analysis of mixing or concentration below the resolution scale. Based on the $Re \sim 6 \times 10^6$ and visual thickness $L \sim 0.1$ m of the separated shear layer at the imaging location, the Kolmogorov scale is estimated as $\lambda_K \sim L/Re^{3/4} \sim 0.82\,\mu$m. Therefore, the total range of scales is $L/\lambda_K \sim 1.3 \times 10^5$ whereas our images capture the range of scales $L/150\,\mu\text{m} \sim 0.67 \times 10^3$. Therefore, the full range of scales spans approximately five decades, however, our imaging resolution (1000×1000 pixels), captures the three upper decades since the pixel resolution scale is 0.1 mm. As we will

show later in section 4, despite the lack of full resolution, the resolved range of scales is able to capture a part of the spectral $-5/3$ inertial behaviour.

3. The Multiscale-Minima Meshless (M^3) method for generalized fractal analysis

Our objects of interest are scalar interfaces which are the isosurfaces, or contours in two dimensions, of a passive scalar turbulent field:

$$c(\boldsymbol{x}, t) = \text{constant}, \tag{3.1}$$

where c is a scalar of interest for any point location $\boldsymbol{x}$ and at any time t. These scalars could represent such quantities as the concentration of certain species, density or refractive index. After identification of a scalar interface, analysis of geometrical properties can be conducted (e.g. Sreenivasan & Prasad 1989; Prasad & Sreenivasan 1990; Catrakis *et al.* 2002; Dasi *et al.* 2007). An important concept in the study of the geometric multiscale behaviour of turbulence is the analysis of fractional (non-integral) dimensions, also known as fractal dimensions, pioneered by the studies of Mandelbrot (1975) and Sreenivasan & Meneveau (1986) as discussed in § 1.

It is important to keep in mind that different definitions and methods for evaluating the fractal dimension can give different results (e.g. Sreenivasan 1991). In this study, we will utilize two methods for evaluating the fractal dimension where one method is the M^3 method recently developed by Catrakis (2008) and the other method is conventional box counting that has been frequently used in the past. The typical starting point in many earlier studies of the fractal aspects of turbulence has been the assumption of statistical self-similarity. This assumes that there is an object in d-dimensional Euclidean space with a constant fractal dimension D_d. However, more generally, one may need to consider the generalized fractal dimension $D_d(\lambda)$ as a function of scale λ as has been pointed out in several studies (e.g. Takayasu 1982; Catrakis 2000) because such a generalized fractal dimension does not constrain *a priori* the behaviour to be self-similar. This allows therefore for possible scale dependence, and includes self-similarity as a special case, so that

$$0 \leqslant D_d(\lambda) \leqslant d. \tag{3.2}$$

Whereas in many practical cases the generalized fractal dimension is at least as large as the topological dimension d_t, i.e. $D_d(\lambda) \geqslant d_t$, we note that there are exceptional cases where the dimension at certain scales may be smaller than the topological dimension such as a circle in a large reference area which can have dimension values less than unity, for example, at large scales for a sufficiently large reference area. For turbulent scalar interfaces, however, unless one utilizes an extraordinarily large reference area, we expect that $d_t \leqslant D_d(\lambda) \leqslant d$.

There are various definitions and methods for evaluating the dimension. It is known that different definitions and different methods may give different results for the dimension (e.g. Sreenivasan 1991). Nevertheless, a frequently used approach for studying fractal dimensions in many studies of turbulence has focused on a method known as box counting (e.g. Sreenivasan 1991; Lane-Serff 1993; Dalziel, Linden & Youngs 1999). This method requires the formation of partitions subdividing a square or rectangular reference region into successively smaller boxes. The box count $N_d(\lambda)$ is then computed which measures the number of partition boxes that cover the object at a specified box scale λ. This is then used to evaluate the fractal dimension as

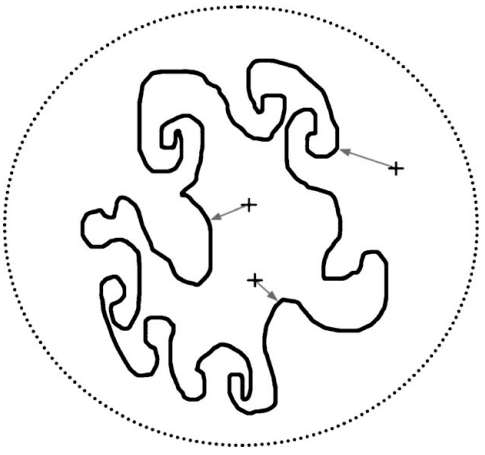

FIGURE 6. This schematic illustration demonstrates the basic idea of the M^3 method for evaluating the generalized fractal dimensions of an object. Random point locations, denoted by crosses, are chosen within the reference area and the shortest distance to the nearest part of the object are computed as indicated by the arrows. Since the M^3 is a meshless approach, the reference boundary can have any imposed shape. In this example a circular boundary is shown.

follows:

$$D_d(\lambda) = -d \log N_d(\lambda)/d \log \lambda. \tag{3.3}$$

This conventional method, therefore, requires the generation of multiple grids, or meshes, at certain resolution scales and then at other refined resolution scales to evaluate the fractal dimension.

An alternative method has been recently developed known as the M^3 method (Catrakis 2008). The M^3 method is a purely meshless method for evaluating fractal dimensions as functions of scale. Validation of this method with theoretical examples is available in the study by Catrakis (2008) with extensive comparisons to conventional box counting. An interesting feature of the M^3 method is that it does not require any type of grid or box subdivision, thus allowing for a purely meshless evaluation of the generalized fractal dimension as a function of scale. The rest of this section will include a brief description of the M^3 method. A full description of the M^3 method can be found in the study of Catrakis (2008). Figure 6 shows a schematic illustartion of the basic idea of the M^3 method which is to identify the shortest-distance scale from a random location to the nearest part of the object of interest, i.e. to the nearest part of the scalar interface.

We will first consider the shortest-distance p.d.f. $g_d(\lambda)$, which is defined as the p.d.f. that λ is the shortest distance from a point at a random location inside a reference region, to the nearest part of an object which in this study is a turbulent interface. The associated probability $g_d(\lambda)d\lambda$ is the probability that the shortest distance is within the range $[\lambda, \lambda + d\lambda]$. The shortest-distance p.d.f. $g_d(\lambda)$ can then be normalized as follows:

$$\int_0^L g_d(\lambda)\,\mathrm{d}\lambda = \int_0^{\lambda_c} g_d(\lambda)\,\mathrm{d}\lambda = 1, \tag{3.4}$$

where $0 \leqslant \lambda \leqslant L$ includes the range of shortest-distance scales for a bounded reference region. The length L represents a characteristic large scale in the bounded reference region. The scale λ_c is defined as the largest shortest-distance scale at $g_d(\lambda)$ is non-zero.

From this it is clear that λ_c is expected to be smaller than the largest characteristic scale L.

Let us consider the cumulative probability integral which is also the distribution function of the shortest-distance scales. This can be viewed as the integral of all the probabilities of all the shortest-distance scales in the range $0 \leqslant \lambda \leqslant \lambda'$. Then the total geometrical probability that the shortest distance is any scale smaller than or equal to $\lambda/2$ is the same as the geometrical probability that a randomly located segment of size λ contains a part of the object. Thus, in one-dimensional, the cumulative distribution function of the shortest-distance scales is equal to the coverage fraction $F_1(\lambda)$:

$$\int_0^{\tilde{\lambda}} g_1(\lambda')\,\mathrm{d}\lambda' = F_1(\lambda). \tag{3.5}$$

We recall that the coverage fraction $F_1(\lambda)$ is defined as the probability that a randomly placed λ-sized segment contains a part of the interface. The shortest-distance scale in the upper limit in (3.5) is, by the geometrical argument stated above, therefore half the size of the one-dimensional coverage element:

$$\tilde{\lambda} = \lambda/2. \tag{3.6}$$

The key relation in (3.5) holds because the total of all the possible probabilities of the shortest-distance scales in the range $0 \leqslant \lambda \leqslant \tilde{\lambda}$, from a random location, is precisely the probability that a randomly placed one-dimensional λ-sized box contains a part of the turbulent interface (Catrakis 2008).

Using the coverage-fraction definition of the generalized fractal dimension, i.e.

$$D_1(\lambda) \equiv 1 - \frac{\mathrm{d}\log F_1(\lambda)}{\mathrm{d}\log\lambda} \tag{3.7}$$

and substituting (3.5), we obtain the generalized fractal dimension as a function of the shortest-distance p.d.f.:

$$D_1(\lambda) = 1 - \frac{\tilde{\lambda} g_1(\tilde{\lambda})}{\int_0^{\tilde{\lambda}} g_1(\tilde{\lambda}')\,\mathrm{d}\tilde{\lambda}'}. \tag{3.8}$$

Figure 7 shows an example of the M^3 method with 3000 random points chosen within a circular domain. Note that in multiple dimensions ($d > 2$), the equivalence in (3.5) does not hold because the shape of the coverage element needed would be multi-dimensional, for example it would be a disc for $d = 2$ or a sphere for $d = 3$, instead of a box. This shows that the concept of a box-based generalized fractal dimension is limiting due to the constraints placed by the shape of the box. One way of resolving this issue is, as stated before, choose a disc, spheres or another multi-dimensional shape as a coverage element. However, a better choice would be one that avoids entirely any constraints as to the shape of the coverage element. This can be done through use of the new purely meshless generalized fractal dimension function $D_d(\lambda)$ which is defined in any d-dimensional space. We can start by defining the shortest-distance cumulative probability function which we denote as $G_d(\lambda)$ as follows:

$$G_d(\lambda) = \int_0^{\lambda} g_d(\lambda')\,\mathrm{d}\lambda'. \tag{3.9}$$

The derivative of the shortest-distance p.d.f. $g_d(\lambda)$ is the shortest-distance p.d.f.: $g_d(\lambda) = d\,G_d(\lambda)/d\lambda$. The cumulative distribution function $G_d(\lambda)$ at a scale λ

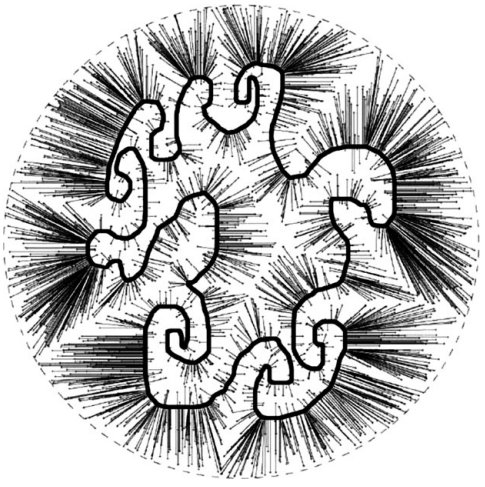

FIGURE 7. Example of the M^3 method with 3000 randomly chosen points within a circular reference area. The random points are represented by small crosses similar to figure 6 and the nearest location to the object is shown using a line segment. The random locations are uniformly chosen within the reference area. The resulting picture shows clusters of locations associated with the multiscale minimal positions for the object.

corresponds to the probability that a random location is at most a distance λ from the nearest part of the object. Its limiting values are $G_d(\lambda \to 0) = 0$ and $G_d(\lambda \to L) = 1$ at the smallest and largest scales, respectively. Recalling our result for $d = 1$ from (3.7) and (3.8) and stating it in terms of the cumulative p.d.f. we can then define by direct analogy a new generalized fractal dimension $D_d(\lambda)$ for the general case, i.e. for any Euclidean dimension d, as follows:

$$D_d(\lambda) \equiv d - \frac{\tilde{\lambda} g_d(\tilde{\lambda})}{\int_0^{\tilde{\lambda}} g_d(\tilde{\lambda}') \mathrm{d}\tilde{\lambda}'} = d - \frac{\mathrm{d} \log G_d(\tilde{\lambda})}{\mathrm{d} \log \tilde{\lambda}}. \tag{3.10}$$

This can be expressed in terms of the scales greater than or equal to by using the normalization equation (3.4), as follows:

$$D_d(\lambda) = d - \frac{\tilde{\lambda} g_d(\tilde{\lambda})}{1 - \int_{\tilde{\lambda}}^{L} g_d(\tilde{\lambda}') \, \mathrm{d}\tilde{\lambda}'}. \tag{3.11}$$

This expression is directly invertible

$$g_d(\tilde{\lambda}) = \frac{d - D_d(\lambda)}{\tilde{\lambda}} \exp\left\{ - \int_{\tilde{\lambda}}^{L} [d - D_d(\tilde{\lambda})] \frac{\mathrm{d}\tilde{\lambda}'}{\tilde{\lambda}'} \right\}. \tag{3.12}$$

Extensive testing of the M^3 method and comparisons to the conventional box-counting technique are available in the study by Catrakis (2008) in which the M^3 method has been formulated, including exact analytical examples illustrating the theory of the M^3 method. It is important to note that since the M^3 method requires placing random points within a specified reference region, some care needs to be placed in choosing a reference region. One possible choice is to take the entire image as the reference region. However, this may affect the resulting dimension. This is due to the fact that there may be a large number of locations outside the fluid interface, which would contribute more to the shortest-distance p.d.f. when the size of the reference region is larger compared to the characteristic large-scale size of the physical interface or object. For transverse slices of flows such as jets which have closed interfaces, this

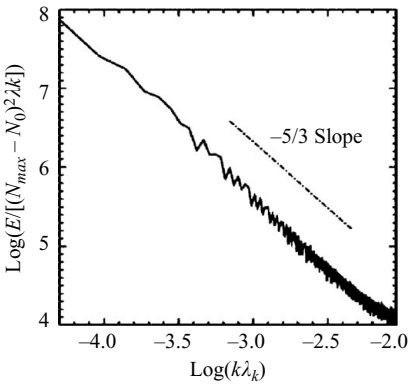

FIGURE 8. This figure depicts the ensemble-averaged normalized scalar power spectrum E of the separated shear layer, with evidence of the $k^{-5/3}$ inertial range, where N_{max} and N_0 denote the concentration values for the pure free stream and ambient fluids, respectively.

ambiguity can be easily avoided if one defines the region enclosed by the interface as the reference region. For shear-layer images, since the interfaces are not closed contours, a reasonable choice for the reference area appears is an interface-fitting reference area of rectangular shape surrounding each individual interface or pair of interfaces. Other choices are possible such as using the interface itself as the boundary, as illustrated for jet flows (e.g. Catrakis 2008).

4. Results on the fractal geometry of separated shear layer interfaces

In this section, we will present the results of our generalized fractal dimension analysis of turbulent shear layers using the M^3 method and the box-counting method. The variable pressure flow facility at UC Irvine was used, as described in § 2, to generate single stream shear layers which were imaged using laser-induced florescence techniques. Spectral analysis of these images shows that even though the images are not fully resolved one is able to capture three decades of scales ranging from the largest scale to smaller scales including a part of the inertial scales. Figure 8 is a plot of the ensemble-averaged power spectrum of the separated shear-layer scalar fields. From this figure one can see that these flow conditions produce the $k^{-5/3}$ power distribution law as expected for fully developed turbulent flows.

Figure 9 is a plot of the ensemble-averaged p.d.f. of the separated shear layer scalar field. The two main locations of local minima in the p.d.f. are used to identify the outer interfaces of the separated shear layer as upper and lower interfaces corresponding respectively to the higher and lower concentration thresholds indicated in figure 9. In figure 10, examples of upper and lower interfaces are shown. An asymmetric intermediate peak in the scalar p.d.f. around $(N - N_0)/(N_{max} - N_0) = 0.6$, where N denotes the concentration with N_{max} and N_0 denoting the free stream and ambient concentration values, respectively, is evident which is consistent with previous studies and is due to the spatial growth of the flow and the corresponding asymmetry in entrainment (e.g. Dimotakis 2005). Figure 11 is a surface plot that assists in visualizing the variations of the normalized threshold values and their relation to the interfaces.

Figure 12(*a*) shows the ensemble-averaged generalized fractal dimension results using the M^3 method for the combined upper and lower interfaces using the interface-fitting rectangular reference area as described below. Figure 12(*b*) shows an example of the combined upper and lower interfaces extracted and the reference

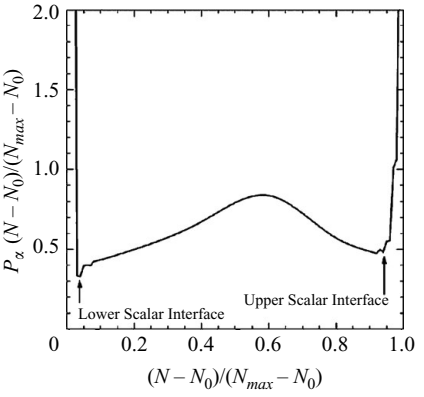

FIGURE 9. Ensemble-averaged p.d.f. of the scalar field of the separated shear layer. The quantity $(N - N_0)/(N_{max} - N_0)$ is the normalized scalar threshold where N denotes the concentration value, i.e. the scalar threshold, with N_0 corresponding to pure ambient air and N_{max} corresponding to the pure free stream air/acetone mixture.

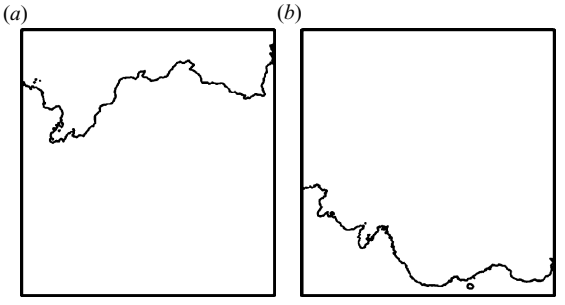

FIGURE 10. Examples of individual upper and lower outer interfaces in the separated shear layer identified from the scalar fields. Image (*a*) depicts an example of an upper interface and image (*b*) shows an example of a lower interface.

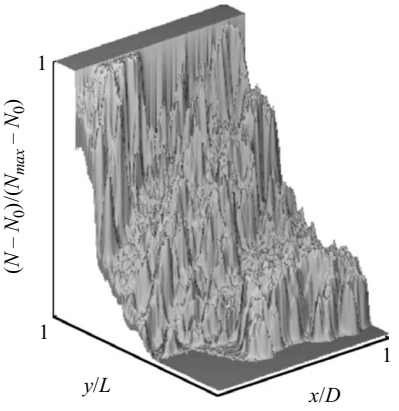

FIGURE 11. This is an example of a surface plot depicting the variations of the scalar field in the separated shear layer. The z-axis of this plot represents the normalized scalar threshold value defined in the x-axis of figure 9. The x- and y-axes of this image are streamwise and transverse positions in the shear layer, respectively, normalized by the maximum corresponding extent of the imaged scalar field region.

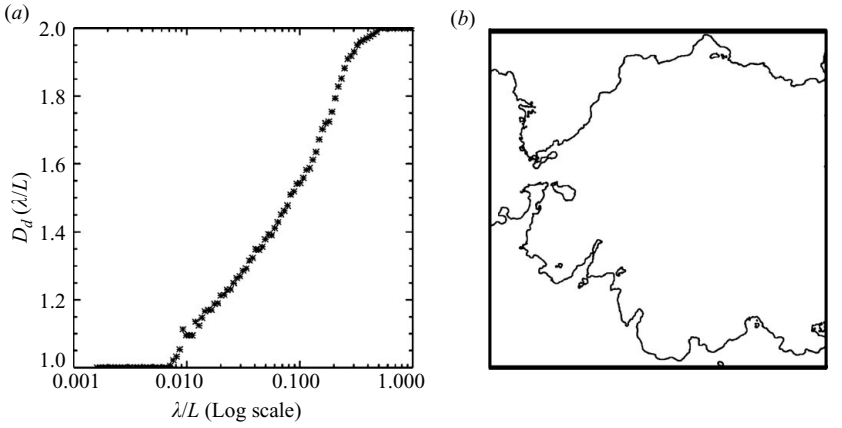

FIGURE 12. (*a*) Ensemble-averaged generalized fractal dimension plot of shear layer upper and lower interfaces using the M^3 method with 100 000 random point locations and using an interface-fitting reference area. (*b*) Example of upper and lower interfaces with the reference area outlined.

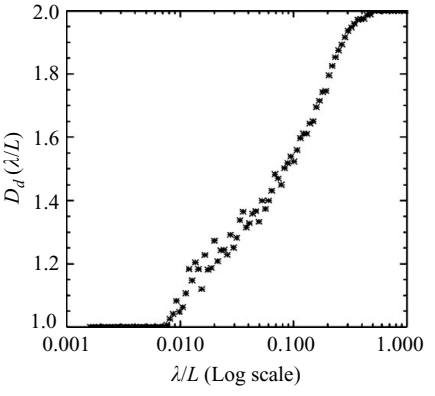

FIGURE 13. Ensemble-averaged generalized fractal dimension versus logarithmic normalized scale for upper and lower interfaces of the separated shear layer using the M^3 method with a reduced number of 10 000 random point locations, in order to explore the effect of the number of point locations on the dimension, and using the interface-fitting reference area in figure 12.

area outlined. We utilized 100 000 random point locations for each realization to generate this generalized fractal dimension plot as well as the related plot in figure 15 discussed below. We denote as interface-fitting rectangular area the boundary region identified by bounding the upper and lower interfaces of the shear layer image and bounding the upstream and downstream sides of the image. The generalized fractal dimension in figure 12 shows strong scale dependence using the M^3 method, with evidence of an approximately linear dependence of the generalized fractal dimension on the logarithmic scale. Specific models for such behaviour have been proposed (e.g. Queiros-Conde 2003). More generally, it is known that such scale dependence can also be the result of finite-Reynolds-number effects (e.g. Catrakis 2000, Catrakis *et al.* 2002).

Figure 13 shows the effect of reducing the number of point locations from 100 000 to 10 000 in the M^3 method. Comparing figures 12 and 13, we see evidence of convergence with the 100 000 point locations as compared to 10 000 point locations

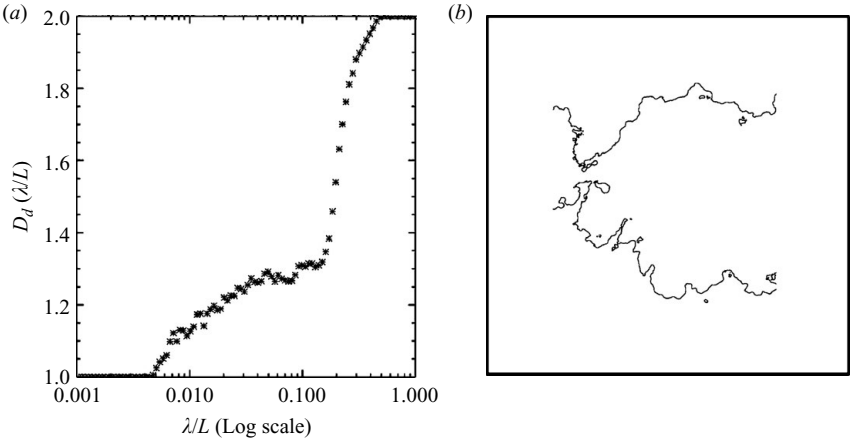

FIGURE 14. (*a*) Ensemble-averaged generalized fractal dimension plot of shear layer upper and lower interfaces using the M^3 method with 100 000 random point locations and a large reference area to explore the effect of increasing the reference area on the dimension. (*b*) Example of outer interfaces with the reference area outlined.

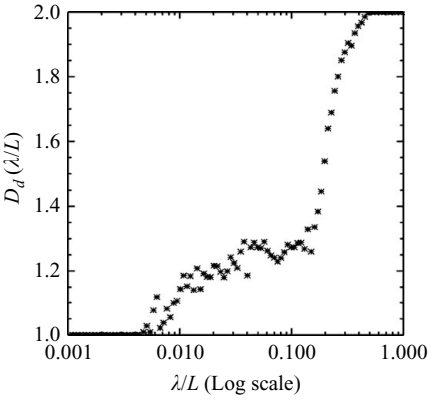

FIGURE 15. Ensemble-averaged generalized fractal dimension versus logarithmic normalized scale for upper and lower interfaces of the separated shear layer using the M^3 method with a reduced number of 10 000 random point locations, in order to explore the effect of the number of point locations on the dimension, for the larger reference area used in figure 14.

since the fluctuations in the dimension versus logarithmic normalized scale diminish significantly from 10 000 point locations to 100 000 point locations. In order to explore the possible effect of the reference area on the generalized fractal dimension in the M^3 method, figures 14(*a*) and 15 show the generalized fractal dimension for 100 000 point locations and for 10 000 point locations, respectively, using a larger reference area as depicted in figure 14(*b*). The effect of this increased reference area seems to be the creation of an approximate plateau near a dimension $D \sim 1.3$, i.e. fractal behaviour based on the M^3 method. We conclude therefore that the behaviour based on the M^3 method can depend on the reference area utilized.

To compare the M^3 method to the conventional box-counting technique, figure 16(*a*) shows the ensemble-averaged generalized fractal dimension using box counting for upper and lower interfaces with interface-fitting rectangular boundaries. As with the

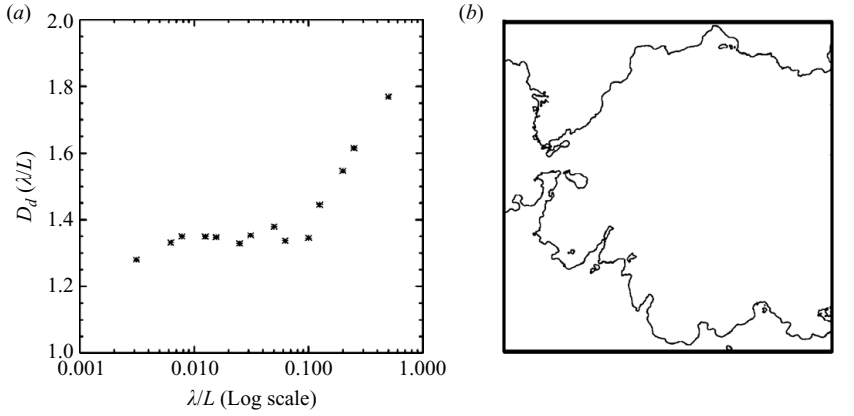

FIGURE 16. (*a*) Ensemble-averaged fractal dimension plot for shear layer upper and lower interfaces using the box-counting method using an interface-fitting rectangular reference area. (*b*) Example of one of the shear layer interface pairs used in the analysis with the reference area outlined.

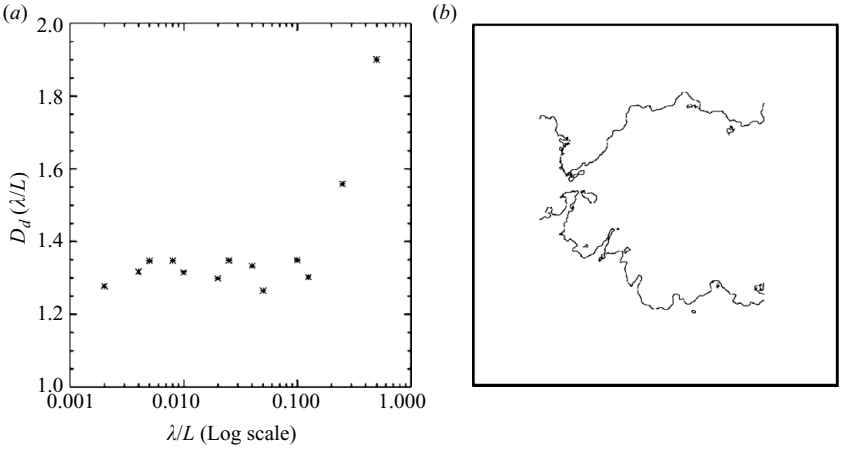

FIGURE 17. (*a*) Ensemble-averaged fractal dimension plot of shear layer upper and lower interfaces using the box-counting method using a larger reference area. (*b*) Example of one of the shear layer interface pairs used in the analysis with the reference area outlined.

previous plots, figure 16(*b*) depicts an example of upper and lower interfaces with the reference area outlined. The corresponding plot of the generalized fractal dimension shows evidence of fractal behaviour with a plateau near a dimension $D \sim 1.3$ over a range of intermediate scales in the shear layer. In order to explore the possible effect of the reference area on the generalized fractal dimension using the box-counting technique, figure 17 was created. The effect of this change in reference area appears to increase the range of scales in which fractal behaviour is seen but without affecting the plateau value of the dimension.

Using the M^3 method and the box-counting method, we also show some sample results for individual realizations of turbulent interfaces with regard to the generalized fractal dimension. As observed above in the context of figures 12 and 14, we see that larger reference areas can affect the dimension behaviour especially for the M^3

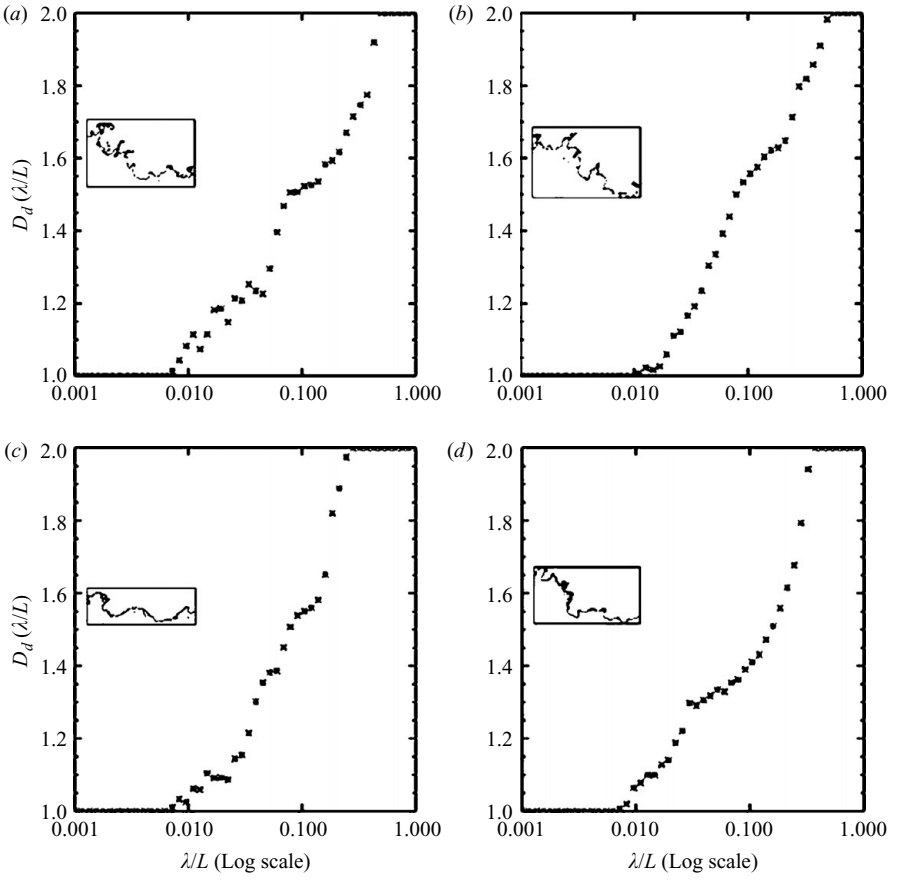

FIGURE 18. Examples of fractal dimension plots for individual realizations of the lower interfaces in the shear layer using the M^3 method and an interface-fitting reference area made to fit closely around the interface in each case.

method. For this reason, we show some sample results for individual scalar interface realizations with the interface-fitting rectangular reference area around each interface. Figures 18 and 19 show examples of the fractal dimension plots for individual realizations of shear layer interfaces extracted from the shear layer images, using the M^3 method and the box-counting method, respectively. For reference, the scalar interface and reference area are depicted in the plot. As with the ensemble-averaged results shown in figures 12 and 14, we see in the individual-realization sample results in figures 18 and 19 that there is strong scale dependence of the dimension on the basis of the M^3 method but there is evidence of a constant dimension on the basis of the box-counting method. In both cases, as expected in comparison to the ensemble-averaged results, there are fluctuations in the dimension behaviour depending on the particular realization.

To explore scalar threshold effects on the generalized fractal dimension, i.e. for internal interfaces as well as for outer interfaces, we have used both the M^3 method and the box-counting method with an interface-fitting rectangular boundary region for interfaces at different scalar thresholds. Figures 20 and 21 show the ensemble-averaged dimension of interfaces for various threshold levels, using the M^3 method and the box-counting method, respectively. Figures 20(*a*) and 21(*a*) show the dimension

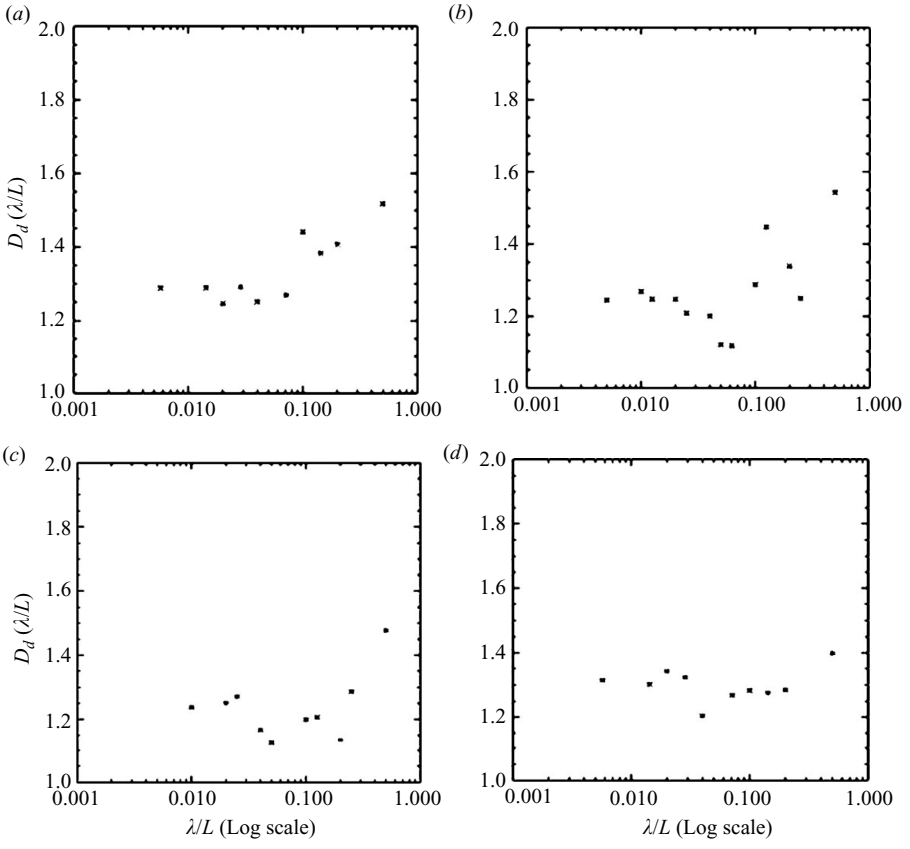

FIGURE 19. Examples of fractal dimension plots for individual realizations of lower interfaces in the shear layer using the box-counting method and an interface-fitting rectangular reference area around each interface, corresponding to the results by the M^3 method in figure 18.

behaviour for the lower outer interfaces, using the scalar threshold as indicated in the scalar p.d.f. in figure 9, for the M^3 method and for the box-counting method, respectively. Figures 20(*b*) and 21(*b*) show the dimension behaviour for internal interfaces at an intermediate normalized scalar threshold value of 0.2, based on the values in the scalar p.d.f. in figure 9, for the M^3 method and for the box-counting method, respectively. Figures 20(*c*) and 21(*c*) are for internal interfaces at a different intermediate normalized scalar threshold value of 0.6, based on the scalar p.d.f. in figure 9, for the M^3 method and for the box-counting method, respectively. Figures 20(*d*) and 21(*d*) are generated for the upper outer interfaces using the scalar threshold as in the scalar p.d.f. in figure 9, for the M^3 method and for the box-counting method, respectively. These results are overall qualitatively similar with the results presented above in figures 12 and 16. The box counting results in figures 21(*a–d*) and 23 discussed below indicate a range of values of fractal dimension $D \sim 1.2$–1.4 depending on the scalar threshold.

Figures 22 and 23 depict the entire three-dimensional plots of the generalized fractal dimension as a function of logarithmic scale and normalized scalar threshold value, using the M^3 method and the box-counting method, respectively. These surface plots indicate that across a wide range of scalar thresholds the dimension behaviour

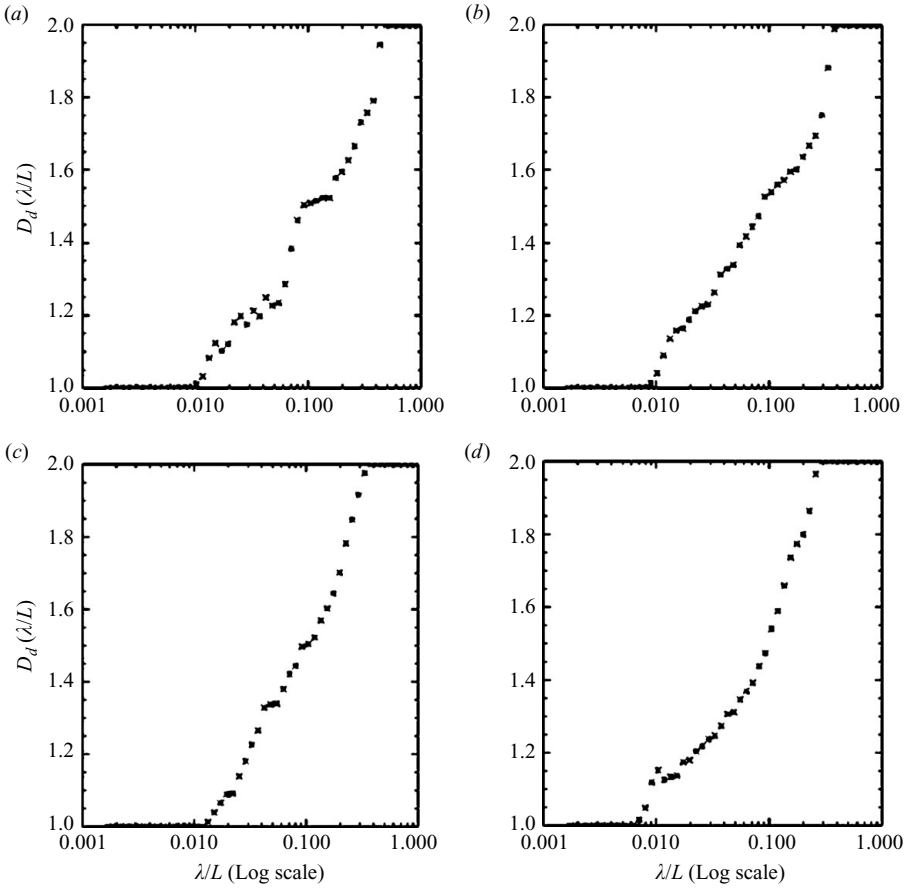

FIGURE 20. Examples of ensemble-averaged fractal dimension plots of shear layer interfaces using the M^3 method and an interface-fitting rectangular reference around each interface for various concentration thresholds. (*a*) The average fractal dimension for the lower concentration threshold; (*d*) the behaviour for the upper threshold value; (*b*) and (*c*) plots of the fractal dimension for intermediate threshold values.

is qualitatively similar to the results obtained in figures 12 and 16, respectively, for the M^3 method and for the box-counting method. Thus, in figure 22, the M^3 method shows evidence of scale-dependent behaviour in the generalized fractal dimension for various scalar thresholds. An approximately linear variation of the generalized fractal dimension as a function of logarithmic scale is evident for various thresholds in figure 22 using the M^3 method. In contrast, the box-counting results in figure 23 indicate a nearly constant dimension with values in the range $D \sim 1.2$–1.4 depending on the threshold for a wide range of scalar thresholds.

Thus, as also observed above in the comparison between figures 12 and 16, there appears to be evidence of fractal behaviour on the basis of the box-counting method in figure 23 but evidence of strong scale dependence is found on the basis of the M^3 method in figure 22. At least for the present flow conditions, these two methods give different results on the dimension behaviour. We note, as discussed above, that each of the two methods has its own merits. The box-counting method has been

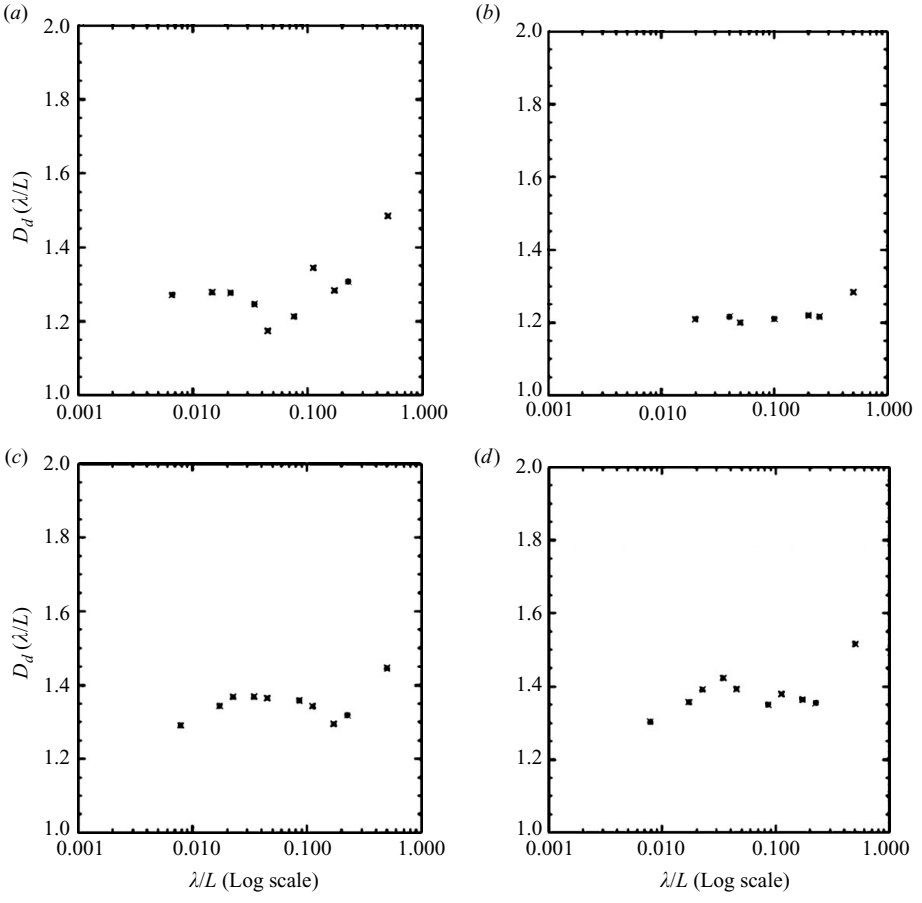

FIGURE 21. Examples of ensemble-averaged fractal dimension plots of shear layer interfaces using the box-counting method and an interface-fitting reference boundary for interfaces at various concentration thresholds. (*a*) The average fractal dimension for the lower concentration threshold; (*d*) the behaviour for the upper threshold value; (*b*) and (*c*) plots of the fractal dimension for intermediate threshold values.

frequently used in previous studies by various researchers and thus it is important to have box-counting results for comparisons to prior works. In this regard, we note that the box-counting dimension value range of $D \sim 1.2$–1.4 in this study is in good agreement with various prior studies (e.g. Sreenivasan 1991). The recently developed M^3 method (Catrakis 2008) eliminates the need for grids or box subdivisions and thus the presently observed strong scale dependence based on the M^3 method, for the interface-fitting boundary regions, may be interpreted as behaviour free from any effects of box subdivisions. We have observed above that increasing the size of the reference region in the M^3 method for the present data can result in behaviour indicative of fractal constant-dimension behaviour. Regarding the general issue of geometrical scale dependence versus self-similarity, we note that it has been shown theoretically that scale dependence can be the result of finite-Reynolds-number effects that can mask intrinsic power-law behaviour even for several decades of power-law scaling (Catrakis 2000).

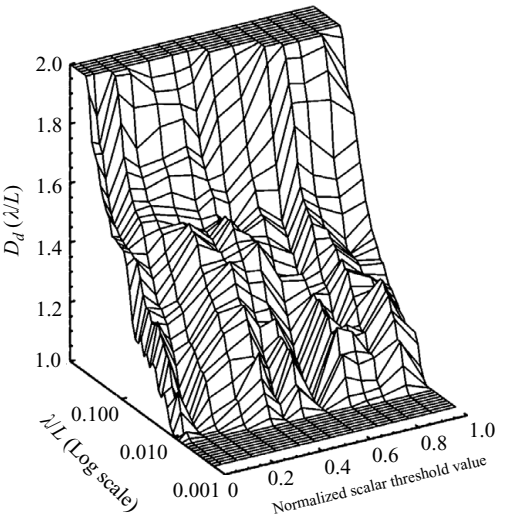

FIGURE 22. A three-dimensional plot of generalized fractal dimension computed using the M^3 method versus λ/L (in Log scale) versus normalized scalar threshold defined as $(N - N_0)/(N_{max} - N_0)$ where N_0 is the lower scalar value and N_{max} is the upper scalar value. Notice the general trend of scale-dependent generalized fractal dimension is present at various scalar threshold values.

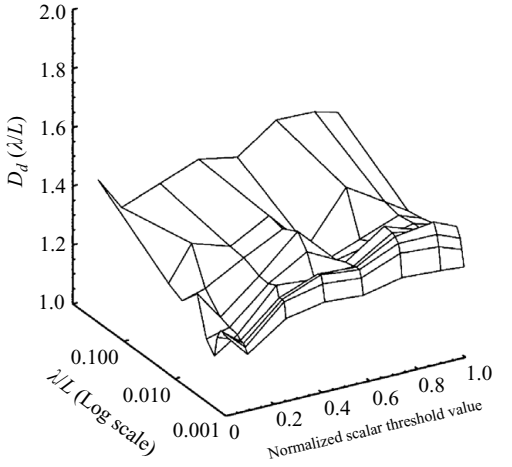

FIGURE 23. A three-dimensional plot of box-counting results, corresponding to the M^3 method results in figure 22, of the generalized fractal dimension as a three-dimensional plot showing the dimension versus λ/L (in Log scale) versus the normalized scalar threshold defined as $(N - N_0)/(N_{max} - N_0)$ where N_0 is the lower scalar value and N_{max} is the upper scalar value.

5. Conclusions

In this study an investigation of the geometrical properties of scalar turbulent interfaces derived from large-*Re* separated shear layer scalar field data was conducted. The three new key elements in this work are that the separated shear layer geometry has not been previously explored for fractal aspects, the large-Reynolds-number conditions are higher than many previous studies of fractals (e.g. Catrakis *et al.* 2002), as well as the use and comparison of both the box-counting method and

the Multiscale-Minima Meshless method with the latter recently developed (Catrakis 2008). In the present study, the power spectrum of experimentally generated shear layers showed evidence of the $k^{-5/3}$ spectral behaviour. Outer scalar interfaces were identified on the basis of the p.d.f. of the scalar field. For the fractal aspects, we utilized two methods as it is known that different methods may lead to different fractal aspects. We used the recently developed method for fractal analysis known as the M^3 method because it does not require the use of grids. We also used the conventional box-counting approach as it has been frequently employed in various past studies and thus we compared the dimension behaviour between the two methods.

For the outer interfaces, our results using the M^3 method revealed strong scale dependence of the generalized fractal dimension with approximately linear variation of the generalized fractal dimension as a function of logarithmic scale, for interface-fitting reference areas. However, for larger reference areas, evidence of an approximate plateau with a dimension of $D \sim 1.3$ is found for the M^3 method. Using the conventional box-counting approach, we also find evidence of a plateau with a constant dimension of $D \sim 1.3$, without a noticeable effect of the reference area, that is in agreement with previous studies that also used box counting. The effects of scalar threshold were also examined and our findings for internal interfaces are qualitatively similar to those for outer interfaces. The overall range of fractal dimension values is $D \sim 1.2$–1.4 depending on scalar threshold. The present findings indicate that the fractal aspects of scalar interfaces in separated shear layers at large Reynolds number with $-5/3$ spectral behaviour are dependent on the method employed for identifying the dimension, with scale dependence for the M^3-based dimension and self-similarity for the box-based dimension.

It is important to appreciate that there are various definitions of the geometrical, or fractal, dimension that each have their own merits and are known to give different results for given objects (e.g. Sreenivasan 1991). Different definitions of the dimension have different utilities that can be employed for multiscale modelling of the interfacial geometry. In the present work, we have focused on two definitions of the dimension for the following reasons. The M^3-based dimension eliminates the need for grids and can be theoretically related to the p.d.f. of generalized level crossing scales as shown in a recent study in which the method has been formulated and tested (Catrakis 2008). The box-counting dimension has been widely used in various studies of fractal dimensions in turbulence and thus it is important, for comparison purposes, to have results available for it as well. It should be kept in mind that fractal dimensions in turbulence are useful for quantifying the area of isosurfaces or perimeter of level sets, for identifying the extent of self-similarity or scale dependence, and for probing the distribution of interfacial scales. Different definitions of the dimension relate in different ways to the isosurface area, to the extent of self-similarity or scale dependence and to the level crossing scales (e.g. Sreenivasan 1991; Catrakis 2008), so that the particular modelling choice as well as utility of the definition of the dimension depends therefore on its connection to the isosurface area, to self-similarity or scale dependence and to the level crossing scales. Theoretical aspects of these connections are available in the studies of Sreenivasan (1991) and Catrakis (2008).

We are grateful to S. Piatrovich, A. Freeman, J. Shockro, A. Wachtor, R. Sokolowski and R. Aguirre for their contributions at various stages of this work. We are also grateful to the Referees for their insightful comments.

REFERENCES

Aguirre, R. C. & Catrakis, H. J. 2005 On intermittency and the physical thickness of turbulent fluid interfaces. *J. Fluid Mech.* **540**, 39–48.

Anselmet, F., Djeridi, H. & Fulachier, L. 1994 Joint statistics of a passive scalar and its dissipation in turbulent flows. *J. Fluid Mech.* **280**, 173–197.

Antonia, R. A. & Sreenivasan, K. R. 1977 Log-normality of temperature dissipation in a turbulent boundary layer. *Phys. Fluids* **20** (11), 1800–1804.

Bermejo-Moreno, I. & Pullin, D. I. 2008 On the non-local geometry of turbulence. *J. Fluid Mech.* **603**, 101–135.

Bilger, R. W. 2004 Some aspects of scalar dissipation. *Flow Turbul. Combust.* **72**, 93–114.

Bisset, D. K., Hunt, J. C. & Rogers, M. M. 2002 The turbulent/non-turbulent interface bounding a far wake. *J. Fluid Mech.* **451**, 381–410.

Brethouwer, G., Hunt, J. C. R. & Nieuwstadt, F. T. M. 2003 Micro-structure and Lagrangian statistics of the scalar field with a mean gradient in isotropic turbulence. *J. Fluid Mech.* **474**, 193–225.

Catrakis, H. J. 2000 Distribution of scales in turbulence. *Phys. Rev.* E **62**, 564–578.

Catrakis, H. J. 2004 Turbulence and the dynamics of fluid interfaces with applications to mixing and aero-optics. In *Recent Research Developments in Fluid Dynamics,* vol. 5, pp. 115–158. Transworld Research Network Publishers.

Catrakis, H. J. 2008 The multiscale-minima meshless (M^3) method: a novel approach to level crossings and generalized fractals with applications to turbulent interfaces. *J. Turbul.* **9**(22), 1–25.

Catrakis, H. J., Aguirre, R. C. & Ruiz-Plancarte, J. 2002*a* Area-volume properties of fluid interfaces in turbulence: scale-local self-similarity and cumulative scale dependence. *J. Fluid Mech.* **462**, 245–254.

Catrakis, H. J., Aguirre, R. C., Ruiz-Plancarte, J., Thayne, R. D., McDonald, B. A. & Hearn, J. W. 2002*b* Large-scale dynamics in turbulent mixing and the three-dimensional space-time behaviour of outer fluid interfaces. *J. Fluid Mech.* **471**, 381–408.

Dahm, W. J. A. & Southerland, K. B. 1997 Experimental assessment of Taylor's hypothesis and its applicability to dissipation estimates in turbulent flows. *Phys. Fluids* **9** (7), 2101–2107.

Dalziel, S. B., Linden, P. F. & Youngs, D. L. 1999 Self-similarity and internal structure of turbulence induced by Rayleigh–Taylor instability. *J. Fluid Mech.* **399**, 1–48.

Dasi, L. P., Schuerg, F. & Webster, D. R. 2007 The geometric properties of high-Schmidt-number passive scalar isosurfaces in turbulent boundary layers. *J. Fluid Mech.* **588**, 253–277.

Dimotakis, P. E. 2005 Turbulent mixing. *Annu. Rev. Fluid. Mech.* **37**, 329–356.

Frederiksen, R. D., Dahm, W. J. A. & Dowling, D. R. 1996 Experimental assessment of fractal scale similarity in turbulent flows. Part 1. One-dimensional intersections. *J. Fluid Mech.* **327**, 35–72.

Frederiksen, R. D., Dahm, W. J. A. & Dowling, D. R. 1997 Experimental assessment of fractal scale similarity in turbulent flows. Part 2. Higher-dimensional intersections and non-fractal inclusions. *J. Fluid Mech.* **338**, 89–126.

Frederiksen, R. D., Dahm, W. J. A. & Dowling, D. R. 1998 Experimental assessment of fractal scale similarity in turbulent flows. Part 4. Effects of Reynolds and Schmidt numbers. *J. Fluid Mech.* **377**, 169–187.

Joseph, D. D. & Preziosi, L. 1989 Heat waves. *Rev. Mod. Phys.* **61**, 41–73.

Jumper, E. J. & Fitzgerald, E. J. 2001 Recent advances in aero-optics. *Prog. Aerospace Sci.* **37**, 299–339.

Kyrazis, D. 1993 Optical degradation by turbulent free shear layers. *Optical Diagnostics in Fluid and Thermal Flow* (ed. S. S. Cha & J. D. Trolinger), pp. 170–181. Society of Photo-Optical Instrumentation Engineers.

Lane-Serff, G. F. 1993 Investigation of the fractal structure of jets and plumes. *J. Fluid Mech.* **249**, 521–534.

Latz, M. I., Juhl, A. R., Ahmed, A. M., Elghobashi, S. E. & Rohr, J. 2004 Hydrodynamic stimulation of dinoflagellate bioluminescence: a computational and experimental study. *J. Exp. Bio.* **207**, 1941–1951.

Mandelbrot, B. B. 1975 On the geometry of homogeneous turbulence, with stress on the fractal dimension of the isosurfaces of scalars. *J. Fluid Mech.* **72** (2), 401–416.

Meneveau, C. & Sreenivasan, K. R. 1991 The multifractal nature of turbulent energy dissipation. *J. Fluid Mech.* **224**, 429–484.

Morris, S. & Foss, J. 2003 Turbulent boundary layer to single-stream shear layer: the transition region. *J. Fluid Mech.* **494**, 187–221.

Pope, S. B. 1988 Evolution of surfaces in turbulence. *Intl J. Engng Sci.* **26**, 445–469.

Pope, S. B. 2000 *Turbulent Flows*. Cambridge University Press.

Prasad, R. R. & Sreenivasan, K. R. 1990 Quantitative three-dimensional imaging and the structure of passive scalar fields in fully turbulent flows. *J. Fluid Mech.* **216**, 1–34.

Queiros-Conde, D. 2003 A diffusion equation to describe scale- and time-dependent dimensions of turbulent interfaces. *Proc. R. Soc. Lond.* A **459**, 3043–3059.

Schumacher, J. & Sreenivasan, K. R. 2003 Geometric features of the mixing of passive scalars at high Schmidt numbers. *Phys. Rev. Lett.* **91**, 4501–4504.

Schumacher, J., Sreenivasan, K. R. & Yeung, P. K. 2005 Very fine structures in scalar mixing. *J. Fluid Mech.* **531**, 113–122.

Sreenivasan, K. R. 1985 On the fine-scale intermittency of turbulence. *J. Fluid Mech.* **151**, 81–103.

Sreenivasan, K. R. 1991 Fractals and multifractals in fluid turbulence. *Annu. Rev. Fluid. Mech.* **23**, 539–600.

Sreenivasan, K. R. 1999 Fluid turbulence. *Rev. Mod. Phys.* **71**, S383–S395.

Sreenivasan, K. R. 2004 Possible effects of small-scale intermittency in turbulent reacting flows. *Flow Turbul. Combust.* **72**, 115–141.

Sreenivasan, K. R. & Meneveau, C. 1986 The fractal facets of turbulence. *J. Fluid Mech.* **173**, 357–386.

Sreenivasan, K. R., Prabhu, A. & Narasimha, R. 1983 Zero-crossings in turbulent signals. *J. Fluid Mech.* **137**, 251–272.

Sreenivasan, K. R. & Prasad, R. R. 1989 New results on the fractal and multifractal structure of the large Schmidt number passive scalars in fully turbulent flows. *Physica* D **38**, 322–329.

Sreenivasan, K. R., Ramshankar, R. & Meneveau, C. 1989 Mixing, entrainment and fractal dimensions of surfaces in turbulent flows. *Proc. R. Soc. Lond.* A **421**, 79–108.

Stanek, M., Raman, G., Ross, J. A., Odedra, J., Peto, J., Alvi, F. & Kibens, V. June 2002 High frequency acoustic suppression: the role of mass flow, the notion of superposition, and the role of inviscid instability. In *American Institute of Aeronautics and Astronautics (AIAA) 8th Aeroacoustics Conference and Exhibit, AIAA Paper 2002–2404*, Breckenridge, CO.

Su, L. K. & Clemens, N. T. 1999 Planar measurements of the full three-dimensional scalar dissipation rate in gas-phase turbulent flows. *Exp. Fluids* **27**, 507–521.

Takayasu, H. 1982 Differential fractal dimension of random walk and its applications to physical systems. *J. Phys. Soc. Jpn.* **51**, 3057–3064.

Thurber, M. C. & Hanson, R. K. 1999 Pressure and composition dependences of acetone laser-induced fluorescence with excitation at 248, 266, and 308 nm. *Appl. Phys.* B **69**, 229–240.

Trouvé, A. & Poinsot, T. 1994 The evolution equation for the flame surface density in turbulent premixed combustion. *J. Fluid Mech.* **278**, 1–31.

Villermaux, E. & Innocenti, C. 1999 On the geometry of turbulent mixing. *J. Fluid Mech.* **393**, 123–147.

Warhaft, Z. 2000 Passive scalars in turbulent flows. *Annu. Rev. Fluid. Mech.* **32**, 203–240.